DEVELOPMENT OF A FLOW SOLVER EMPLOYING LOCAL ADAPTATION BASED ON MULTISCALE ANALYSIS ON B-SPLINE GRIDS

F. Bramkamp, J. Ballmann
Lehr- und Forschungsgebiet für Mechanik, Templergraben 64, 52056 Aachen, Germany
bramkamp@lufmech.rwth-aachen.de

S. Müller
Institut für Geometrie und Praktische Mathematik, Templergraben 55, 52056 Aachen, Germany
mueller@igpm.rwth-aachen.de

ABSTRACT

In the framework of this paper, the basic concepts and preliminary results of a new flow solver, which employs locally h-adaptive grids with hanging nodes, are presented. The new method consists of an integrated framework, including a novel grid generation using B-Splines, advanced adaptation criteria based on multiscale analysis and a flow solver which is capable to operate on arbitrary unstructured meshes. Several test cases for stationary, inviscid flows have been studied to validate the basic method. Firstly, the so called Ringleb flow has been considered to assess the spatial accuracy of the scheme. Secondly, the flow around a wing section has been investigated in subsonic as well as in transonic Mach number regime. The results of the present scheme are in good agreement with experimental data and other flow solvers.

INTRODUCTION

The outlined investigations are a project part of the collaborative research center SFB401: *Modulation of Flow and Fluid/Structure Interaction at Airplane Wings*, RWTH Aachen, Germany [1], whose aim it is to efficiently simulate the viscous flow around flexible wings in cruise and high-lift configuration. The aerodynamics of high-lift configurations is extremely complex. Amongst others, confluent boundary layers and wakes, turbulent separated flow regions and compressibility effects are encountered. In order to resolve these effects by a numerical scheme, a strongly heterogeneous discretization is required to account for the different scales. A uniform discretization that is determined by the finest scale is not appropriate, since it requires a prohibitive amount of memory resources and computational time. Therefore, algorithms have to be developed with computational effort and memory requirements that are proportional to the complexity of the underlieing problem, i.e., only in regions where small-scales physical effects are present the discretization has to be refined, and elsewhere a much coarser discretization will be sufficient. This task is being addressed adequately by locally adaptive schemes. Adaptive methods efficiently utilize available resources and may provide more accurate and reliable solutions. Further, the grid generation process is greatly facilitated, since the initial -coarse-mesh has solely to be adjusted to the geometry but not to the flow solution. Efficient and reliable adaptive strategies require an integrated framework consisting of the components: grid generation, adaptation and flow solver. These items will be addressed within this paper.

The paper is organized as follows. First, the basic concepts regarding grid generation and adaptation criteria will be outlined briefly. Next, the flow solver will be described in greater depth. Finally, several test cases will be discussed to verify the accuracy of the basic scheme.

GRID GENERATION

The computational domain is initially tessellated by a coarse multiblock structured grid. As basic element types, quadrilaterals and hexahedra are employed in two and three space dimensions, respectively. The mesh is locally adapted to the solution according to the principle of h-adaptation, see Fig. 1. Hanging nodes, which occur due to local refinement are maintained, i.e. no transition elements are introduced. Hence, the adaptation remains local and the basic element type is being preserved. The grid generation is based on a B-Spline technique [2], which is particularly suited for adaptive algorithms, since it provides a very efficient way to represent the mesh at low memory costs. Each block of the structured mesh is represented by a B-Spline function of the form

$$\mathbf{x}(\mathbf{s}) = \sum_{\mathbf{i}} \mathbf{P_i} \prod_{l=1}^{d} N_{i_l}^m(s_l) \qquad (1)$$

with control points $\mathbf{P_i}$. d denotes the dimension of the space. The order m of the B-Spline function N_l^m is chosen as 4. This technique offers various advantages:

- B-Splines provide excellent adaptability to boundaries.
- Since the grid is stored as a function only a few control points are necessary to represent each block. Geometric quantities required by the flow solver may consistently be evaluated at any location within the domain. In particular, a truly nested sequence of locally adapted cells can be provided, which is required by the applied adaptation criteria, based on multiscale analysis.
- The B-Spline approach can be combined with various grid generation techniques, e.g. algebraic, elliptic or hyperbolic grid generation methods, by means of B-Spline interpolation and approximation.

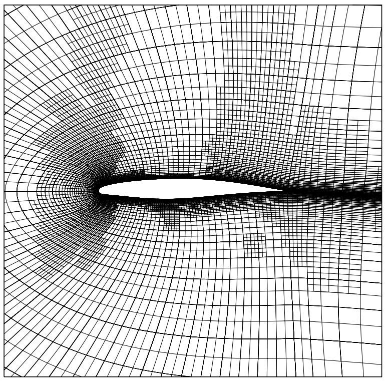

Figure 1: Locally adapted grid; SFB401 cruise configuration, $M_\infty = 0.76$, $\alpha = 0°$

ADAPTATION CRITERIA

The mesh adaptation is performed by means of multiscale techniques similar to those used in data compression. Here we follow a strategy originally developed by A. Harten [3]. Starting point is a sequence of *nested* grids $\mathcal{G}_j := \{\Omega_{j,i}\}_i$, not necessarily structured, and corresponding averages $\overline{\mathbf{u}}_j := \{\mathbf{u}_{j,i}\}_{i\in\mathcal{G}_j}$, $j = 0,\dots,L$, see Fig. 2. By means of this sequence, we successively decompose the averages $\overline{\mathbf{u}}_L$ on the finest level L into a sequence of averages $\overline{\mathbf{u}}_0$ on the coarsest level and details $\overline{\mathbf{d}}_j$, $j = 0,\dots,L-1$, see Fig. 3. The averages and the details are interpreted as L_2–scalar products of the conservative quantities $\mathbf{u}$ and the L_1–weighted box function

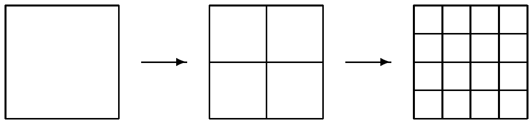

Figure 2: Sequence of nested grids

$$\begin{tikzcd} \overline{\boldsymbol{u}}_L \arrow[r, leftrightarrow] \arrow[dr, leftrightarrow] & \overline{\boldsymbol{u}}_{L-1} \arrow[r, leftrightarrow] \arrow[dr, leftrightarrow] & \cdots \arrow[r, leftrightarrow] \arrow[dr, leftrightarrow] & \overline{\boldsymbol{u}}_1 \arrow[r, leftrightarrow] \arrow[dr, leftrightarrow] & \overline{\boldsymbol{u}}_0 \\ & \overline{\boldsymbol{d}}_{L-1} & \cdots & \overline{\boldsymbol{d}}_1 & \overline{\boldsymbol{d}}_0 \end{tikzcd}$$

Figure 3: Multiscale Transformation

$\varphi_{j,i} := \frac{1}{|\Omega_{j,i}|}\chi_{\Omega_{j,i}}$ and appropriate wavelet functions $\psi_{j,i,e},\ e \in E$, i.e.,

$$\mathbf{u}_{j,i} := (\mathbf{u},\varphi_{j,i})_{L_2(\Omega)},\ \mathbf{d}_{j,i,e} := (\mathbf{u},\psi_{j,i,e})_{L_2(\Omega)}$$

where E indicates the set of subcells corresponding to $\Omega_{j,i}$. For reasons of simplicity we assume a regular refinement, i.e. the cardinality of E always corresponds to the number of subcells minus one. The construction of the wavelet functions $\psi_{j,i,e}$ is subject to certain constraints, namely, reversibility of multiscale decomposition, local support of wavelet functions, vanishing moments and stability.

The detail coefficients can be interpreted as differences, which become negligibly small in regions where the solution is sufficiently smooth. We introduce the set of significant details $\mathcal{D}_\varepsilon := \{(j,i,e)\ :\ |d_{j,i,e}| > \varepsilon_j\}$ where $\varepsilon_j = 2^{j-L}\varepsilon$ is a level–dependent threshold value.

Since the flow field at hand is supposed to be heterogeneous, the number of significant detail coefficients, i.e., $N_D := \#\mathcal{D}_\varepsilon$, is much smaller than the number of averages N_L corresponding to the finest scale. The ultimate goal is to perform the multiscale transformation such that the complexity with respect to computational time as well as memory requirements corresponds to N_D rather than N_L. For details see [4].

By means of $\mathcal{D}_\varepsilon$ we determine a locally refined grid with hanging nodes denoted by $\mathcal{G}_\varepsilon$, i.e., $\bigcup_{(j,i)\in\mathcal{G}_\varepsilon}\Omega_{j,i}$ and the corresponding sequence of averages $\overline{\mathbf{u}}_{L,\varepsilon} := \{\overline{\mathbf{u}}_{j,i}\}_{(j,i)\in\mathcal{G}_\varepsilon}$. The adapted grid $\mathcal{G}_\varepsilon$ is determined by proceeding from coarse to fine. If there exists a significant detail $\mathbf{d}_{j,i,e},\ e \in E$ corresponding to the cell $\Omega_{j,i}$ the grid is locally refined.

GOVERNING EQUATIONS

In the present study, the fluid motion is governed by the time dependent Euler equations, which can be expressed in conservation form for a control volume Ω with boundary $\partial\Omega$ and outward unit normal $\mathbf{n}$ as:

$$\int_{\Omega} \frac{\partial \mathbf{u}}{\partial t} dV + \oint_{\partial\Omega} \mathbf{F}^c(\mathbf{u})\mathbf{n}\, dS = \mathbf{0} \qquad (2)$$

with initial values $\mathbf{u}(\mathbf{x}, t_0) = \mathbf{u}_0(\mathbf{x})$, $\mathbf{x} \in \Omega$ and boundary conditions $\mathbf{u}(\mathbf{x}, t)|_{\partial\Omega} = \mathcal{B}(\mathbf{x}, t)$, $\mathbf{x} \in \partial\Omega$. The state vector of conserved flow variables $\mathbf{u}$ and the physically conservative flux $\mathbf{F}^c$ are defined by

$$\mathbf{u} = \begin{pmatrix} \rho \\ \rho\mathbf{v} \\ \rho e_{tot} \end{pmatrix}, \ \mathbf{F}^c(\mathbf{u}) = \begin{pmatrix} \rho\mathbf{v} \\ \rho\mathbf{v} \circ \mathbf{v} + p\mathcal{I} \\ \rho h_{tot}\mathbf{v} \end{pmatrix} \qquad (3)$$

where ρ denotes the density, p the static pressure, $\mathbf{v}$ the velocity vector, e_{tot} the total energy and h_{tot} the total enthalpy. The system is closed by the equation of state for a perfect gas $p = \rho(\gamma - 1)(e_{tot} - 1/2\,|\mathbf{v}|^2)$, where γ is the ratio of specific heats, which is taken as 1.4.

FINITE VOLUME METHOD

Grid Concept and Data Structure

The discretization of the governing equations (2) is based on a cell centered finite volume scheme. Caused by the occurance of hanging nodes, the grid is treated as a fully unstructured mesh with arbitrary polygonal/polyhedral control volumes in two and three space dimensions, respectively.

The data structure of the flow solver is primarily based on the faces of the grid. A face based data structure has the important benefit that there are no limitations on the number of faces, which can be connected to a cell. Further, the evaluation of fluxes and their distribution to cells can efficiently be implemented by sweeps over the faces.

Calculation of Conservative Fluxes

The conservative fluxes are determined by solving quasi-one-dimensional Riemann problems at the cell interfaces. Various approximate Riemann solvers have been incorporated. Within the present paper, the scheme due to Roe [5] has been applied. The conservative flux function is calculated by utilizing the rotational invariance of the Euler equations $\mathbf{F}^c(\mathbf{u})\,\mathbf{n} = \mathcal{T}^{-1}(\mathbf{n})\,\mathbf{F}^c(\tilde{\mathbf{u}})$, where $\tilde{\mathbf{u}} = \mathcal{T}(\mathbf{n})\,\mathbf{u}$ and $\mathcal{T}$ represents the rotational matrix. The surface integral of the fluxes is evaluated using a midpoint rule, which is consistent with a second order scheme in space.

Reconstruction

In order to obtain second-order accuracy in space, a linear representation of the conservative variables is reconstructed on each control volume Ω_i

$$w(\mathbf{x})|_{\Omega_i} = w_i + \phi_i \nabla w_i \cdot (\mathbf{x} - \mathbf{c}_i) \qquad (4)$$

where w represents the reconstructed flow variable, w_i its mean value at the centroid $\mathbf{c}_i$ of Ω_i and ϕ_i denotes the limiter function. The gradient ∇w_i is obtained by employing the Green-Gauss theorem or a least squares method.

Green-Gauss gradient computation

A widely employed linear reconstruction technique is based on the computation of the gradient by the Green-Gauss theorem which is applied to compute the average gradient of w over the surface of a bounding control volume

$$\nabla w_i = \frac{1}{\Gamma_i} \oint_{\partial\Gamma_i} w\,\mathbf{n}\, d\partial\Gamma_i \qquad (5)$$

where Γ_i denotes a control volume, which is defined by the centroids of the neighbouring cells of Ω_i, which represent the support of the reconstruction. The Green-Gauss technique is applied in two space dimensions only, since the evaluation of the surface integral requires a certain ordering of the nodes, which is difficult to implement for arbitrary grids in three space dimensions.

Least-squares gradient computation

Another method to determine the gradient of w is based on a multi-dimensional Taylor series expansion around the centroid of Ω_i

$$w_i + \nabla w_i \cdot (\mathbf{x}_j - \mathbf{c}_i) = w_j \Rightarrow \mathcal{A}\nabla\mathbf{w}_i = \Delta\mathbf{w}_i \qquad (6)$$

where

$$\mathcal{A} = \begin{bmatrix} \Delta x_1 & \Delta y_1 & \Delta z_1 \\ \vdots & \vdots & \vdots \\ \Delta x_{N_i} & \Delta y_{N_i} & \Delta z_{N_i} \end{bmatrix}, \ \Delta\mathbf{w}_i = \begin{pmatrix} \Delta w_1 \\ \vdots \\ \Delta w_{N_i} \end{pmatrix} \qquad (7)$$

with $\Delta(\bullet)_j = (\bullet)_j - (\bullet)_i$, $j \in N_i$. N_i is the set of neighbouring cells of Ω_i, which support the reconstruction of w. In practice, eq. (7) represents an overdetermined system of equations for the gradient of w_i. It is solved in a least squares sense utilizing a Householder transformation. This technique can be applied in two as well as in three space dimensions, respectively.

Monotonicity Enforcement

In order to avoid oscillations in the vicinity of local extrema and discontinuities, limiter functions with TVD property are used. The limiter from Venkatakrishnan [6] is employed which is defined as follows:

$$\phi_{i,g} = \begin{cases} \dfrac{w_{i,g}^{+^2} + 2w_{i,g}^{+}w_{i,g}^{-} + \epsilon}{w_{i,g}^{+^2} + w_{i,g}^{+}w_{i,g}^{-} + 2w_{i,g}^{-^2} + \epsilon} & \text{, if } w_{i,g}^{-} \neq 0 \\ 1 & \text{, if } w_{i,g}^{-} = 0 \end{cases} \tag{8}$$

with

$$\begin{aligned} w_{i,g}^{-} &= w_g - w_i, \\ w_{i,g}^{+} &= \begin{cases} w_i^{max} - w_i, & \text{if} \quad w_{i,g}^{-} > 0 \\ w_i^{min} - w_i, & \text{if} \quad w_{i,g}^{-} < 0 \end{cases} \\ w_i^{max} &= max_{j=1,\dots,N_i}\{w_i, w_j\}, \\ w_i^{min} &= min_{j=1,\dots,N_i}\{w_i, w_j\} \end{aligned}$$

w_g denotes the unlimited reconstructed value of w at the Gauss quadrature point g. The coefficient ϵ is typically set to $\epsilon = 10^{-6}$ in our applications. Since condition (8) has to be fulfilled at each quadrature point of the faces, the final limiter associated with the control volume Ω_i is taken as the corresponding minimum value $\phi_i = min\,(\phi_{i,g})$.

Boundary Conditions

Boundary conditions are imposed in a weak manner via the modification of the conservative fluxes through the boundary faces. At solid walls the contact condition $\mathbf{v} \cdot \mathbf{n} = 0$ yields the normal flux formula

$$\mathbf{F}^c \cdot \mathbf{n} = \begin{pmatrix} 0 \\ p\mathbf{n} \\ 0 \end{pmatrix} \tag{9}$$

where the pressure p is being extrapolated from the interior domain. For external flows, a point vortex correction according to Thomas and Salas [7] is applied at far field boundaries.

Temporal Discretization

The temporal evolution of the flow quantities is computed utilizing an explicit Runge-Kutta scheme. Within the framework of this paper a three step scheme is employed with coefficients chosen for optimal damping of high-frequency errors [8]

$$\alpha_1 = 0.1919, \quad \alpha_2 = 0.4930, \quad \alpha_3 = 1.0$$

Convergence to steady state is accelerated by local time stepping. The local time step Δt_i is calculated based on a first order scheme in space

$$\Delta t_i = CFL \cdot \min_j \left(\frac{|\, l_i^j \,|}{|\, \mathbf{v}_i \mathbf{n}^j \,| + c_i} \right) \tag{10}$$

where c_i is the local speed of sound and l_i^j represents the minimal distance between the jth face of $\partial\Omega_i$ and the centroid of the control volume Ω_i.

RESULTS

In the following, test cases for stationary, inviscid flows are presented to verify the basic method. Since the flow solver has not been fully coupled with the adaptation procedure yet, only structured grids in two space dimensions are employed [9].

Ringleb flow

The Ringleb flow [10] has been used as a test case to assess the spatial accuracy of the scheme. An exact solution of this flow can be obtained by a hodograph transformation. The flow depends on the inverse of the stream function k and the velocity magnitude q. In our application we choose the values $k = 0.4$ and $k = 0.8$ to define the rigid walls, and $q = 0.3$ to define the inlet- and outlet boundaries. The flow is fully subsonic within the domain. The inlet Mach number is 0.3027 and the maximum Mach number reaches 0.8567 at the center of the bottom wall. The error E_{h_j} and the spatial order of the scheme EOC (*Experimental Order of Convergence*) are estimated in the L_1 norm of the Mach number:

$$E_{h_j} = \frac{1}{N_j} \sum_{i=1}^{N_j} \left| f_{h_j} - 1 \right|, \; EOC = \frac{log\left(\dfrac{E_{h_j}}{E_{h_{j+1}}}\right)}{log\left(\dfrac{h_j}{h_{j+1}}\right)}$$

where f_{h_j} represents the ratio of the numerical solution and the exact solution on a grid with the characteristic length scale $h_j = 1/\sqrt{N_j}$; N_j is the number of grid cells. The accuracy analysis was carried out on four different grids with a resolution of 16x4, 32x8, 64x16 and 128x32 cells, respectively. In addition, the grids were distorted randomly in order to assess the sensitivity of the solution with regard to mesh quality, see Fig. 4. Fig. 5 illustrates the Mach number distribution along the bottom wall for three different regular grids. The linear Green-Gauss reconstruction method has been employed. For the highest resolution, the maximum error between the

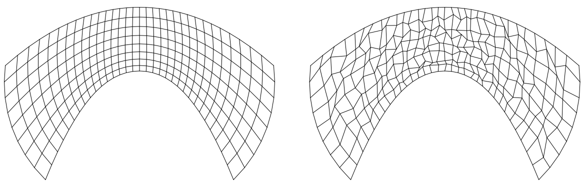

Figure 4: Ringleb flow: Grids (32x8 cells); left figure: regular grid; right figure: randomly distorted grid

numerical solution and the exact solution is about 0.02%. Fig. 6 shows the error E_{h_j} in the Mach number, depending on the characteristic length scale h_j of the mesh. A constant and a linear reconstruction, based on the Green-Gauss method, have been considered. For the linear reconstruction, the sensitivity of the error with regard to grid distortion is weak. The order of accuracy can be estimated between 2.5-2.9 for the linear reconstruction, see Table 1. The constant reconstruction scheme is numerically less then first order accurate for the considered grids.

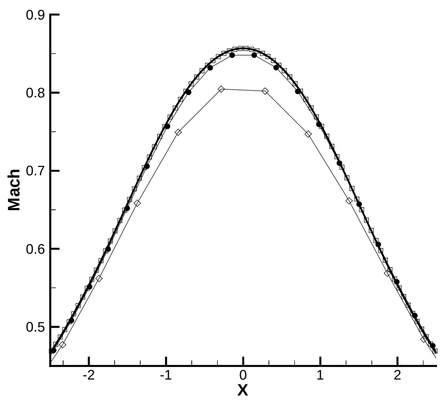

Figure 5: Mach number distribution at bottom wall (partial view); linear Green-Gauss rec. on regular grids; $-$ exact solution, $\square$128x32 cells, $\bullet$32x8 cells, $\diamond$16x4 cells

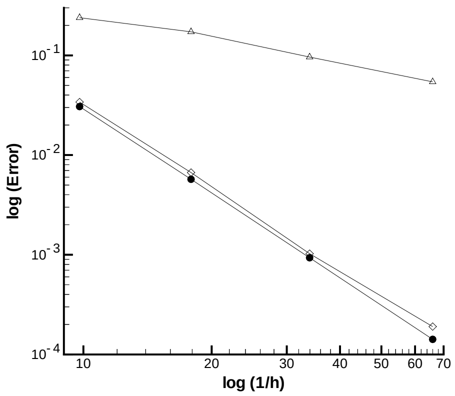

Figure 6: Error in the Mach number. Linear Green-Gauss reconstruction: $\bullet$ regular grid, $\diamond$ distorted grid ; $\triangle$ constant reconstruction (regular grid)

	EOC		
grid	linear rec. regular	linear rec. distorted	constant rec. regular
32x8	2.79	2.70	0.543
64x16	2.83	2.93	0.909
128x32	2.84	2.53	0.862

Table 1: Ringleb flow: experimental order of convergence (EOC) for linear reconstruction and constant reconstruction on regular and distorted grids

SFB401 Cruise Configuration

The next test case investigates the flow around the transonic cruise configuration of the collaborative research center SFB401. Results for the following flow conditions are presented:

- *Case I*: $M_\infty = 0.176, \quad \alpha = 0°$;
- *Case II*: $M_\infty = 0.76, \quad \alpha = 0°$,

with $T_\infty = 285K$. In both cases, the grid resolution is 256x32 cells. Numerical computations conducted with the program FLOWer [11] serve as a reference. For *Case I*, experimental data are available as well [12]. Fig. 7 and Fig. 8 show the pressure isolines and the c_p distribution for *Case I*, respectively. The results of the present method are in good agreement with the numerically obtained reference data. On the upper surface of the profile, both schemes slightly overpredict the pressure distribution compared with experimental data. On the lower surface, a better agreement with experimental data is obtained. Fig. 9 and Fig. 10 present the results for *Case II*. The pressure distribution computed with the present scheme is in good agreement with the numerically obtained reference data.

ACKNOWLEDGEMENT

The financial support from the Deutsche Forschungsgemeinschaft (DFG) is gratefully acknowledged.

REFERENCES

[1] Ballmann, J., *Strömungsbeeinflussung und Strömungs-Struktur-Wechselwirkung an Tragflügeln, Erste Ergebnisse des SFB401 der RWTH Aachen*, DGLR-JT99-189, DGLR Jahrbuch 1999

[2] Brakhage, K.H., Müller, S., *Algebraic-Hyperbolic Grid Generation with Precise Control of Intersection of Angles*, Int. J. Numer. Meth. Fluids. To appear

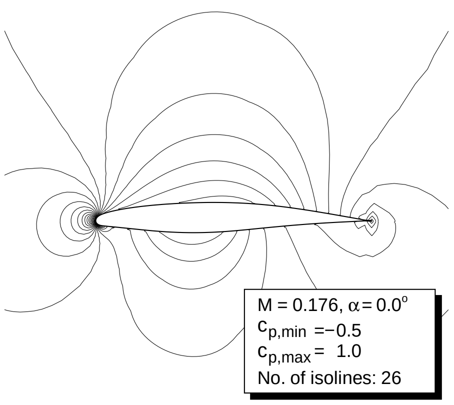

Figure 7: Isobars of the SFB401 cruise configuration, $M_\infty = 0.176$, $\alpha = 0°$, $T_\infty = 285K$

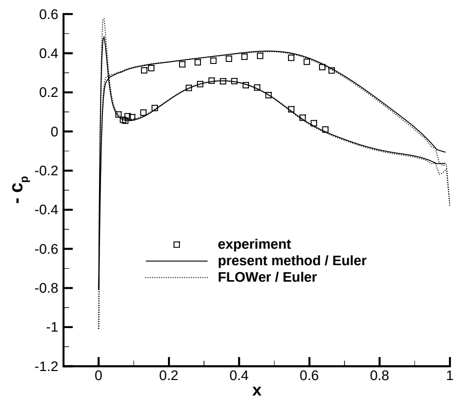

Figure 8: Comparison of the c_p distribution of the SFB401 cruise configuration, $M_\infty = 0.176$, $\alpha = 0°$, $T_\infty = 285K$

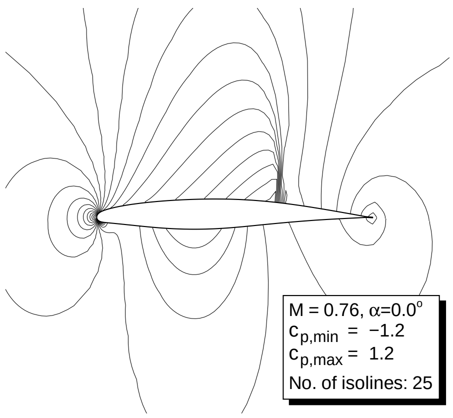

Figure 9: Isobars of the SFB401 cruise configuration, $M_\infty = 0.76$, $\alpha = 0°$, $T_\infty = 285K$

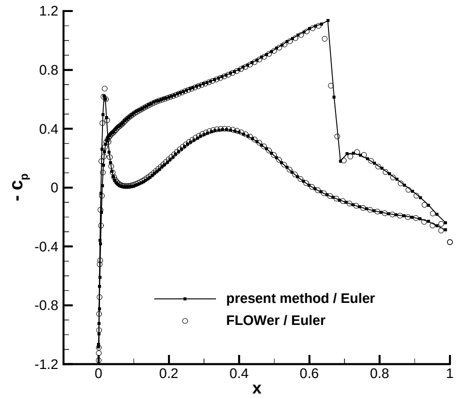

Figure 10: Comparison of the c_p distribution of the SFB401 cruise configuration, $M_\infty = 0.76$, $\alpha = 0°$, $T_\infty = 285K$

[3] Harten, A., *Multiresolution algorithms for the numerical solution of hyperbolic conservation laws*, Comm. Pure Appl. Math. 12, vol. 48 (1995), 1305–1342

[4] Gottschlich–Müller, B., Müller, S., *Adaptive Finite Volume Schemes for Conservation Laws based on Local Multiresolution Techniques*, in: Hyperbolic Problems: Theory, Numerics, Applications, eds. M. Fey and R. Jeltsch, Birkhäuser, 1999, pp. 385–394

[5] Roe, P.L., *Approximate Riemann Solvers, Parameter Vectors, and Difference Schemes*, J. Comp. Phys, 43, 1981, pp. 357–372

[6] Venkatakrishnan, V., *Convergence to Steady State Solutions of the Euler Equations on Unstructured Grids with Limiters*, J. Comp. Phys., 118, 1995, pp. 120–130

[7] Thomas, J.L., Salas, M.D., *Far–Field Boundary Conditions for Transonic Lifting Solutions to the Euler Equations*, AIAA J., 24, 1986, pp. 1074–1080

[8] Tai, C.H., Sheu, J.H., van Leer, B., *Optimal Multistage Schemes for Euler Equations with Residual Smoothing*, AIAA J., 33, 1995, pp. 1008–1016

[9] Hesse, M., *Aspekte der elliptischen Gittergenerierung*, Lehr- und Forschungsgebiet für Mechanik, RWTH Aachen, 1999

[10] Ringleb, F., *Exakte Lösung der Differentialgleichung einer adiabatischen Gasströmung*, ZAMM, 20(4), 1940, pp. 185–198

[11] Becker, K., Kroll, N., Rossow, C.C., Thiele, F., *Numerical Flow Calculations for Complete Aircraft - the Megaflow Project*, DGLR-JT98-225, DGLR Jahrbuch 1998, pp. 355–364

[12] Kurek, J., *Experimentelle Untersuchung der ebenen Referenzkonfiguration des SFB 401*, Institut für Luft- und Raumfahrt, RWTH Aachen, Germany, June 1999